Neural Networks 123 (2020) 273–287

Contents lists available at ScienceDirect

Neural Networks

journal homepage: www.elsevier.com/locate/neunet

2019 Special Issue

Cuneate spiking neural network learning to classify naturalistic texture stimuli under varying sensing conditions

Udaya B. Rongala [a,b,c,d,*], Alberto Mazzoni [a,d], Anton Spanne [c], Henrik Jörntell [c], Calogero M. Oddo [a,d,*]

[a] The BioRobotics Institute, Sant'Anna School of Advanced Studies, 56127 Pisa, Italy
[b] Department of Linguistics and Comparative Cultural Studies, Ca' Foscari University of Venice, 30123 Venice, Italy
[c] Neural Basis of Sensorimotor Control, Department of Experimental Medical Science, Lund University, SE-221 84 Lund, Sweden
[d] Department of Excellence in Robotics & AI, Scuola Superiore Sant'Anna, Pisa, Italy

ARTICLE INFO

Article history:
Available online 9 December 2019

Keywords:
Spiking neural network
Neurorobotics
Cuneate neurons
Primary afferents
Tactile sensing
Synaptic weight learning

ABSTRACT

We implemented a functional neuronal network that was able to learn and discriminate haptic features from biomimetic tactile sensor inputs using a two-layer spiking neuron model and homeostatic synaptic learning mechanism. The first order neuron model was used to emulate biological tactile afferents and the second order neuron model was used to emulate biological cuneate neurons. We have evaluated 10 naturalistic textures using a passive touch protocol, under varying sensing conditions. Tactile sensor data acquired with five textures under five sensing conditions were used for a synaptic learning process, to tune the synaptic weights between tactile afferents and cuneate neurons. Using post-learning synaptic weights, we evaluated the individual and population cuneate neuron responses by decoding across 10 stimuli, under varying sensing conditions. This resulted in a high decoding performance. We further validated the decoding performance across stimuli, irrespective of sensing velocities using a set of 25 cuneate neuron responses. This resulted in a median decoding performance of 96% across the set of cuneate neurons. Being able to learn and perform generalized discrimination across tactile stimuli, makes this functional spiking tactile system effective and suitable for further robotic applications.

1. Introduction

1.1. Objectives of the study

Creating a better understanding of learning paradigms, by which mammals and humans process sensory information, could pave way to engineer effective and efficient sensory solutions for both robotics and neuroprosthetics applications (Dario et al., 2005; Service, 2014; Yang et al., 2016). Considering the sense of touch, given the complexity and variation of the tactile inputs that the brain receives during frequent unpredictable interactions with the dynamic world, the human nervous system should adapt a functional mechanism in unfolding these tactile representations.

In this direction of understanding, we aim to realize a functional tactile system by integrating computational neuron models and learning algorithms along with tactile sensory systems, that will allow us exploit the robust and effective way of dimensionality reduction that happens in tactile sensing: from abundant sensory information across the skin to fewer useful dimensions such as categories describing the qualities associated to tactile interaction. This sequentially leads to learn and represent tactile stimuli, under dynamic sensing conditions.

1.2. Background work

Focusing on neuro-physiology of the sense of touch, in the last four decades several researchers investigated the characteristics and functional role of primary afferent sensors, in transducing the complex contact dynamics between the skin and the external world (Abraira & Ginty, 2013; Johansson & Flanagan, 2009; Pruszynski & Johansson, 2014; Weber et al., 2013). A step further, other research studies proposed various techniques by which this abundant primary afferents information is processed in cuneate neurons (Bengtsson, Brasselet, Johansson, Arleo, & Jörntell, 2013; Jörntell et al., 2014; Suresh et al., 2017) and further how such tactile information is represented in higher levels of the brain (Bensmaia, Denchev, Dammann, Craig, & Hsiao, 2008;

* Corresponding authors.
E-mail addresses: udayabhaskar.rongala@santannapisa.it, udaya_bhaskar.rongala@med.lu.se (U.B. Rongala), calogero.oddo@santannapisa.it (C.M. Oddo).

https://doi.org/10.1016/j.neunet.2019.11.020
0893-6080/

Genna et al., 2018; Mountcastle & Henneman, 2017; Oddo et al., 2017).

In the field of robotics, spiking neural networks were increasingly used to process sensory-motor information in order to achieve efficient and robust learning of surrounding physical environment. Spiking neuron models emulate spatio-temporal spike patterns (group of binary events) from input sensory information. These spike patterns contain both frequency (spike rate) and time (precise spike timing) related information which can be transferred to other neurons in a network using dynamic synaptic connections. Learning these synaptic connections based on previous experiences incrementally over time, will enable a specific network to evolve creating representation of complex input dynamics. Therefore, adopting bio-inspired synaptic and neuron learning paradigms has the potential to enable to mimic the functionality of the brain (Kasabov, 2018). Specifically, in the field of neuro-robotic tactile sensing there were studies that encoded data from various tactile sensors into spike responses emulating primary afferents and further used this neuromorphic spike data to classify tactile stimuli such as braille dots, textures, geometric orientations (Bologna et al., 2013; Friedl, Voelker, Peer, & Eliasmith, 2016; Lee, Kukreja, & Thakor, 2017) or for bionic limb prostheses (Oddo et al., 2016; Osborn et al., 2018). Some research studies presented simulation models of primary afferents (PA) with millisecond precision (Saal, Delhaye, Rayhaun, & Bensmaia, 2017), and other ones successfully modeled multi-layer neuron models based on neuro-physiology data to successfully classify edge orientations under varying sensing conditions (Hay & Pruszynski, 2018) or emulated learning mechanisms of high order brain structures (Chou, Bucci, & Krichmar, 2015).

Previously, we have built and validated a neuromorphic tactile sensor system (Rongala, Mazzoni, & Oddo, 2017) by which we were successful in decoding 10 naturalistic tactile stimuli, based on the precise spike-time information of individual PA response, under different sensing conditions. Later, we have established a cuneate neuron (CN) model and synaptic learning mechanism based on intrinsic membrane dynamics and synaptic weight distribution as observed in *in vivo* recordings (Rongala et al., 2018).

The main objective of this study has been to construct a bio-inspired tactile system, that could learn and represent stimulus specific input tactile features under generalized sensing condition. Towards this objective, we follow an integrated approach where (1) we generate population of PA responses from our tactile sensory system. (2) Adopt the synaptic learning mechanism and cuneate neuron models for population of PA inputs, to generate an ensemble of CN networks. (3) Validate the cuneate neuron responses (based on post-synaptic learning), by decoding stimulus under varied sensing conditions. (4) Further validate the generalized decoding capabilities of a population of CNs.

2. Materials and methods

In this research study we have two phases of network evaluations:

(a) *Synaptic learning phase*: The raw data from biomimetic tactile sensors (for given stimulus) was encoded into primary afferent spike responses (1st order neurons) and projected onto cuneate neurons (2nd order neurons), through randomly distributed excitatory synaptic seed weights. A synaptic learning rule (calcium activity dependent plasticity rule) was adapted to achieve feature specific synaptic end weight distribution, from an initial randomly distributed synaptic seed weight distribution (Figs. 1A and 3C).

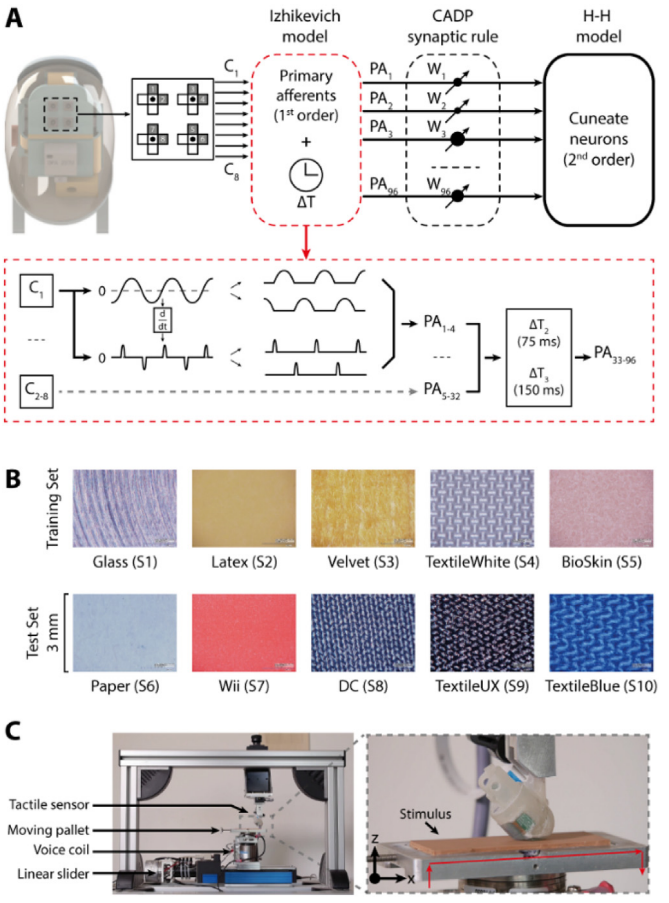

Fig. 1. Methods. (A) Structure of multi-layer spiking neural network. A physical tactile sensor was used to recreate primary afferent like spike responses using Izhikevich neuron model. Sensory data was filtered (as shown in insert) to replicate coding strategies of different afferents (SA-like, FA-like). These primary afferent signals were further provided to the cuneate neurons through a specific synaptic weight ($W_{i,n}$). The synaptic weight learning was based on a calcium activity dependent plasticity rule. (B) Naturalistic tactile stimuli. Each strip shows the microscopic image of tactile stimuli presented to the sensor. Top row: five tactile stimuli (S1–S5) that are used in the synaptic learning process. Bottom row: five tactile stimuli (S6–S10) that are used in model validation along with the top row five stimuli. (C) Experiment protocol. A passive touch protocol was followed, where the tactile sensor was fixed, and the stimuli was slid along the sensory surface. This protocol was classified in three main phases: indentation, sliding and retraction.

(b) *Testing phase*: The primary afferent spike trains (for given stimulus) were projected onto cuneate neurons through learnt excitatory synaptic end weights (post-synaptic learning phase). Later, the two-layer spiking neuron models were validated based on the generalized stimulus decoding capabilities (decoding irrespective of sensing conditions) from these cuneate neuron spike responses (Figs. 1A and 3D).

The following material and methods text is sectioned as follows; In Sections 2.1–2.4, we discuss the methods adopted to generate tactile sensory data. In Sections 2.5 and 2.6 we elaborate the neuron models by which tactile sensory information was processed. In Section 2.7, we discuss the network connectivity between 1st and 2nd order neurons. In Sections 2.8–2.10, we describe the synaptic learning mechanisms. In Section 2.11, we describe various statistical methods adopted to validate the two-layer spiking neural networks.

2.1. Tactile sensor

An in-house developed biomimetic fingertip (tactile sensor) was used for these experiments (Oddo, Controzzi, Beccai, Cipriani and Carrozza, 2011). The fingertip encompasses an array of four (in 2 × 2 formation) piezoresistive sensors constructed using MEMS technology. These sensors are placed on a flat rigid bone-like structure for support and encapsulated with compliant silicon (DragonSkin 10, Smooth-on, USA) around the assembly (Fig. 1A). Each of these piezoresistive sensors comprises of four piezo-resistors coupled in a cross-shape structure, constituting 16 sensory channels for single fingertip. The fingertip has a sensing area of 22.3 mm^2. In case of exploratory motion along a single direction, the tethered construction among piezo resistors (cross-structure) delivers a similar response across opposite sensory channels, lone with shift in polarity of the data. Therefore, in this study we consider only 8 of the 16 sensory channel data (shaded channels in Fig. 1A, *C1–C8*). The sensory channels are responsive for both normal and tangential forces, whose precision and robustness was established in some of our previous studies (Oddo et al., 2011; Oddo, Controzzi et al., 2011; Rongala et al., 2017).

2.2. Stimuli

Ten naturalistic textures were used as tactile stimuli (*S1–S10*) for these experiments (Fig. 1B). Five of these stimuli were textiles and the rest were non-textile textures, each of them exhibiting varied physical properties. Each tactile stimulus of dimension 75 × 30 × 2 mm (length × width × height) was fixed onto an aluminum base plate (that of stimulus dimensions) for support. The tactile sensory data corresponding to five textures (Glass, Latex, Velvet, TextileWhite and BioSkin, *S1–S5*) was used for synaptic learning phase and sensory data corresponding to all ten textures (*S1–S10*) was used in testing phase.

2.3. Experimental protocol

A passive touch protocol (Jones & Lederman, 2007) was followed to create the tactile sensory datasets, for which the tactile sensor was fixed secure and stimulus was slid along the surface of the tactile sensor (Fig. 1C). A 2 degree-of-freedom mechatronic platform (Oddo, Beccai et al., 2011; Oddo, Controzzi et al., 2011) was used to perform these experiments (Fig. 1C). The mechatronic platform encompassed a ball-screw mechanism based linear slider (for displacement along *x*-axis, Fig. 2A) and a voice coil actuator (for displacement along *z*-axis, Fig. 2B), offering a resolution of 0.98 μm along *x*-axis and <20 mN of force along *z*-axis (with closed loop force control). The tactile sensor was fastened onto a fixed frame and the stimulus was loaded onto a moving pallet (connected to both linear slide and voice coil) of mechatronic platform (Fig. 1C). In this experimental protocol, we followed a pre-defined trajectory (red line, Fig. 1C) of the moving pallet, allowing three main experimentation phases: *Indentation*, *Sliding* and *Retraction* (Fig. 2). First, the stimulus was indented onto the surface of the tactile sensor (indentation phase) using voice coil, with a specific amount of sensing force. Next, the stimulus was slid along the surface of the sensor (sliding phase) using linear slider, with a given sensing velocity while maintaining a constant sensing force. At the end of sliding phase the stimulus was retracted back from the contact with tactile sensor (retraction phase). We kept a wait time of 1 s–2 s between the transition of these experimental phases.

In this study, each stimulus was investigated under 5 different sensing velocities (5, 10, 15, 20 and 25 mm/s, *V1–V5 respectively*) for a fixed sensing force of 400 mN. For each sensing condition, 10 experimental repetitions were performed to assess the repeatability of our demonstrated system.

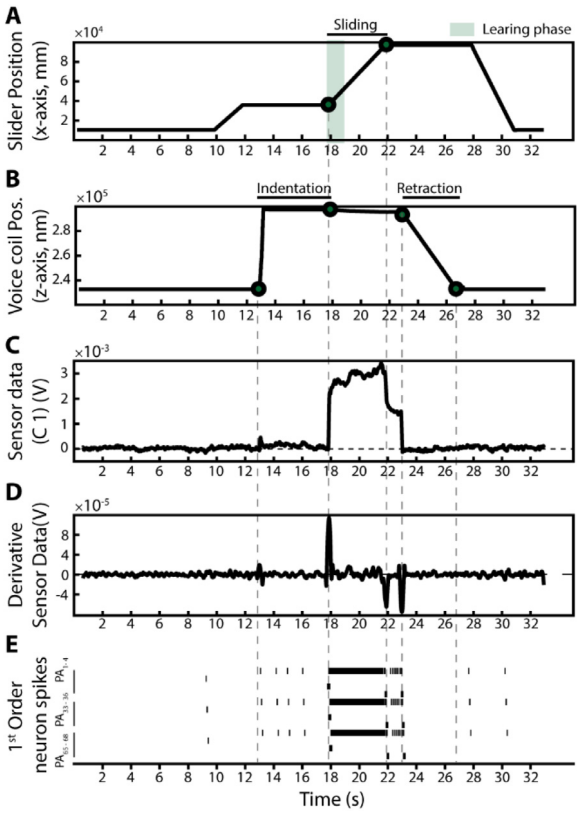

Fig. 2. Experimentation protocol and tactile sensor responses. (A) Trajectory of the slider that maneuver tactile stimuli along horizontal axis (along the surface of the tactile sensor), in a controlled velocity (15 mm/s in this illustration). (B) Trajectory of the voice coil that proceeds tactile stimuli along vertical axis (perpendicular to the tactile sensor) causing controlled indentation for given sensing force (400 mN in this illustration). (C) Raw tactile sensor data for one sensory channel during the illustrated experiment protocol. (D) First derivative of the sensory data. (E) Artificial mechanosensory responses (SA-like and FA-like) corresponding to all the 8 active sensory channels data (C1-8 in Fig. 1A) and their derivative.

2.4. Data processing

The 8 sensory channels (*C1–C8, see* Section 2.1) chosen for this study are further referred as "active sensory channels". The data from each active sensory channel was differentiated to obtain dynamic components (such as transient states) of the sensory data. Both the normal and differentiated sensory signal are split into positive and negative half of the signal and further rectified (Saal et al., 2017). This process resulted in 4 time-varying inputs from each active channel sensory data (Fig. 1A, *insert*). Following this data processing technique, we multiplexed 8 active sensory channel data into 32 sensory inputs. This data filtration process was adopted in order to maximize the sensory information from 8 active sensory channels. Additionally, a two fixed time shifts were added to all the sensory signals to replicate nerve conduction delays as observed in humans and mammals (Johansson & Flanagan, 2009). This signal processing mechanism resulted in a population of 96 sensory input signals from 8 active sensory channels (Fig. 1A), which were fed as input current to the first-order neuron model.

2.5. First-order neuron model to emulate biological primary tactile afferents

Preprocessed tactile sensory data (Fig. 2C) was fed as current input (I_{input}) to the first-order neuron model in order to

Table 1
Izhikevich model parameters.

A	B	C	C_m	a	b	c	d
0.04 s^{-1} V^{-1}	5 s^{-1}	140 V s^{-1}	1 F	0.02 s^{-1}	0.2	−65 mV	8 mV

mimic mechanoreceptor like spike responses (Primary Afferents, PAs, Fig. 2E). We have opted for the Izhikevich neuron model (Izhikevich, 2003) as it exhibits adaptation dynamics, which was a characteristic feature of mechanoreceptors (Johansson & Flanagan, 2009), also with the purpose to compare with previous results of our group that already validated this model (Oddo et al., 2016; Rongala et al., 2017, 2018). However, since the AdEx model (Brette & Gerstner, 2005) is able to emulate Izhikevich neurons firing patterns (Naud, Marcille, Clopath, & Gerstner, 2008) including adaptation dynamics, we expect our results are able to generalize with a full AdEx model.

The Izhikevich neuron model was derived based on two differential Eqs. (1) and (2) discretized using Euler's method. In following equations, v denotes the membrane potential of neuron and u describes its adaptation variable.

$$\dot{v} = Av^2 + Bv + C - u + \frac{I_{input}}{C_m} \tag{1}$$

$$\dot{u} = a(bv - u) \tag{2}$$

When membrane potential reaches a pre-defined voltage threshold ($Spk_{thr} = 30$ mV), a spike was produced following an after-spike reset of membrane potential. This was given by,

$$if\ v \geq 30\ \text{mV}, then \begin{cases} v \leftarrow c \\ u \leftarrow u + d \end{cases} \tag{3}$$

A, B and C are the standard Izhikevich neuron model parameters, whereas a, b, c, and d parameters were chosen in order to reproduce regular spiking behavior (Table 1) (Izhikevich, 2003). This spiking neuron model adaptation enabled us to encode both transient state changes and finer frictional components from the analog sensory data (Fig. 2). Therefore, with help of 1st order neuron model we emulate 96 PA spike responses ($PA_1 - PA_{96}$) from preprocessed sensory data.

2.6. Second-order neuron model to emulate biological cuneate neurons

A calcium based cuneate neuron model was used in this study, that was formulated based on biological cuneate neuron *in vivo* recordings (Rongala et al., 2018). The biological cuneate neurons (CNs) exhibited unique spiking behavior, where they tend to comprise both fast and intermediate dynamics (Bengtsson et al., 2013; Rongala et al., 2018). The fast-dynamic spiking property was observed in initiation of membrane potential to reach the threshold and generate a spike following with after-spike hyperpolarization (I_{spike}). Additional to this spiking behavior CNs also tend to exhibit intermediate spiking dynamics, based on currents from additional ion channels (I_{ion}). These currents do not generate the action potential but tend to influence the action potentials during high input synaptic activity. One such property of these additional currents is to produce high frequency spike bursts. Such spiking behavior was previously observed (Huguenard, 1996; Llinás & Jahnsen, 1982; Molineux et al., 2008), and was partly attributed to the effect of low-threshold voltage gated calcium channels (LVA) and calcium-activated potassium channels (CAP).

Considering both these spiking properties, the cuneate neurons were modeled using conductance based exponential integrate and fire model (Fourcaud-Trocmé, Hansel, van Vreeswijk, & Brunel, 2003) with added calcium dynamics (LVA and CAP). The cuneate neuron membrane potential (V_m) was given by,

$$C_m \frac{dV_m}{dt} = I_L + I_{spike} + I_{ion} + I_{ext} + I_{syn} \tag{4}$$

where, C_m is the membrane capacitance. I_L is the leak current, I_{spike} is the spike currents, I_{ion} is the ion channel currents, I_{syn} is synaptic input current and I_{ext} is external injected currents steps that were used to evaluate the CN responsiveness. These individual currents are given by the following equations,

$$\begin{aligned} I_L &= -\bar{g}_L(V_m - E_L) \\ I_{spike} &= \bar{g}_L \Delta T \exp\left(\frac{V_m - V_t}{\Delta T}\right) \\ I_{ion} &= I_{Ca} + I_K \\ I_{syn} &= g_{max} \sum_i w_i \exp\left(-\tau\left(t - t^*\right)\right)\left(E_{rev,exc} - V_m\right) \\ &\quad + g_{max} w_{inh} \sum_i \exp\left(-\tau\left(t - t^*\right)\right)\left(E_{rev,inh} - V_m\right) \end{aligned} \tag{5}$$

The variable definitions and their respective values were reported in Table 2. The membrane resistance and time constants were chosen as per *in vivo* recordings, whereas the other model parameters were chosen based on an optimization procedure. The parameter optimization was done with an objective to match the model membrane potential to a recorded *in vivo* CN potential, for given step current input (Rongala et al., 2018).

The ion channel currents (I_{ion}), were computed as summation of currents from calcium sensitive LVA channels and CAP channels. These currents are given by following equations,

$$\begin{aligned} I_{Ca} &= -\bar{g}_{Ca} x_{C_{a,a}}^3 x_{Ca,i}\,(V_m - E_{Ca}) \\ I_K &= -\bar{g}_K x_{K_{Ca}}^4 x_{K_{Vm}}^4 (V_m - E_K) \end{aligned} \tag{6}$$

where, $\bar{g}_{Ca}$ and $\bar{g}_K$ are the maximum conductances, E_{Ca} and E_K are the reversal potentials, and $x_{Ca,a}$, $x_{Ca,i}$, $x_{K_{Ca}}$, $x_{K_{Vm}}$ are the activity states of the channels. The conductance and reversal potential values are defined in Table 2, whereas the modeling and optimization of activity states is elaborated in Rongala et al. (2018). Both these ion channels ($x_{C_{a,a}}, x_{C_{a,i}}$) are considered as source of calcium concentration in the cell membrane ($\left[Ca^{2+}\right]$). According to the reasoning depicted in Saarinen, Linne, and Yli-Harja (2008) we construct the total calcium concentration activity based on following Eq. (7).

$$\begin{aligned} \frac{d\left(\left[Ca^{2+}\right]\right)}{dt} &= BCa\bar{g}_{Ca} x_{C_{a,a}}^3 x C_{a,i}\left(V_m - E_{C_a}\right) \\ &\quad + \left(\left[Ca^{2+}\right]_{rest} - \left[Ca^{2+}\right]\right)/\tau_{\left[Ca^{2+}\right]} \end{aligned} \tag{7}$$

The input synaptic current (I_{syn}), was calculated as the summation of both excitatory and inhibitory synaptic currents across all individual primary afferent synapses. The primary afferent spike responses ($PA_1 - PA_{96}$) are transposed as conductances and multiplied with their respective synaptic weights (w_i and w_{inh}, see Sections 2.7–2.10), to serve as input to the CN model Eq. (5). In Eq. (5), g_{max} is the maximum synaptic conductance, E_{rev} is the reversal potential, V_m is the membrane potential and t^* is time of primary afferent activation. The respective values are reported in Table 2.

2.6.1. Local synaptic calcium activity

The synaptic learning process adapted in this study is based on the correlation between total calcium activity in the neuron and the local calcium activity in the individual synapse. The total calcium activity in each CN is considered as a product of total calcium concentration in the cell and an arbitrary constant

Table 2
Second order neuron model parameters.

Parameter	Symbol	Value
Membrane capacitance	C_m	4.270e−11 F
Leak conductance	g_L	8.100e−09 S
Leak reverse potential	E_L	−62.309 mV
Width of the spike (EIF model)	Δ_t	1.3063
Spike threshold (EIF model)	V_t	−57.129 mV
Maximum potassium conductance	g_K	2.022e−08 S
EPSP reversal potential	$E_{rev,exc}$	0 mV
IPSP reversal potential	$E_{rev,inh}$	−80 mV
Potassium reversal potential	E_K	−104.514 mV
Maximum calcium conductance	g_{Ca}	2.082e−08 S
Calcium reversal potential	E_{Ca}	121.436 mV
Conversion factor between calcium current and concentration	B_{Ca}	3.374e−15
Calcium concentration at rest (equilibrium)	Ca^{2+}_{rest}	1.010e−07
Time constant of the calcium concentration leak	$\tau_{Ca^{2+}}$	0.0063
Time constant of the calcium activation state	$\tau_{Ca,a}$	2.722e−04
Time constant of the calcium inactivation state	$\tau_{Ca,i}$	0.0207
Time constant of the potassium calcium dependent activation state	$\tau_{K_{Ca}}$	0.0013
Time constant of the potassium voltage gated activation state	$\tau_{K_{Vm}}$	0.0011
Constant for sigmoid function of intermediate dynamic model	$p_{Ca,a,1}$	−60.8369 mV
Constant for sigmoid function of intermediate dynamic model	$p_{Ca,a,2}$	6.3419 mV^{-1}
Constant for sigmoid function of intermediate dynamic model	$p_{Ca,i,1}$	−68.0100 mV
Constant for sigmoid function of intermediate dynamic model	$p_{Ca,i,2}$	1.3008 mV^{-1}
Constant for sigmoid function of intermediate dynamic model	$p_{K_{Vm},1}$	−64.0785 mV
Constant for sigmoid function of intermediate dynamic model	$p_{K_{Vm},2}$	0.7833 mV^{-1}
Constant for sigmoid function of intermediate dynamic model	$p_{K_{Ca},1}$	2.2166e−07 mV
Constant for sigmoid function of intermediate dynamic model	$p_{K_{Ca},2}$	4.7923e−08 mV^{-1}

($Ca^{2+}_{Tot} = k_{act} * [Ca^{2+}]$), in this study $k_{act} = 1$. The local calcium activity of individual synapse i, for each PA spike input at t^* is given by following kernel (Mazzoni, Panzeri, Logothetis, & Brunel, 2008),

$$Ca^{2+}_{Loc\_i}(t) = \frac{\tau_1}{\tau_d - \tau_r}\left[exp\left(-\frac{t-\tau_l-t^*}{\tau_d}\right) - exp\left(-\frac{t-\tau_l-t^*}{\tau_r}\right)\right] \quad (8)$$

where, τ_r is the raise time (4 ms), τ_d is the decay time (12.5 ms), τ_l is the latency time (0 ms) and τ_1 is the constant (21 ms) to calculate the ratio. The values chosen to define this kernel were based on the biological assumptions to reflect slow after-spike hyperpolarization of CNs, reflecting the calcium concentration in individual synapses (Rongala et al., 2018).

2.7. Network connectivity

Each CN was fully connected to all 96 PA by means of both excitatory synapses (blue triangles, Fig. 3A) and inhibitory synapses (red triangle, Fig. 3A). Each PA input was projected onto the CN as an individual excitatory synapse. Whereas, responses across all PAs were grouped into a single inhibitory synaptic input to the CN (Rongala et al., 2018). The magnitude of post-synaptic potential projected on a CN for given PA input, is dependent on its excitatory and inhibitory synaptic weights (w_i, w_{inh}). In our model, the synaptic weights are gain factor that vary from 0.001 to 1. The total synaptic current input (I_{syn}) to a CN is given by Eq. (5).

During synaptic learning phase, the CN and synaptic learning models (see Section 2.10) were presented with PA responses associated to five stimuli (S_1–S_5) for a given sensing velocity (25, 20, 15, 10, 5 mm/s, $V1$–$V5$) and synaptic seed weight distribution (SW_1–SW_5, see Section 2.8). Based on these input configurations ("SW distribution" and "sensing velocity" of input stimuli), post-synaptic learning we achieve a feature specific synaptic end weight distribution (post-synaptic learning weight distribution). Such synaptic end weight (EW) distribution allows a unique combination of PA inputs to be relayed onto CN, leading to a distinctive CN responses. Therefore, based on combination of all 5 sensing velocities and 5 seed weight configurations, we attain 25 varied EW distributions (Fig. 3B, C) resulting in an **ensemble of 25 CN networks** (CN_1–CN_{25}).

For testing phase, all the 25 CNs were presented with PA responses associated to 10 naturalistic stimuli (S_1–S_{10}) for a given sensing velocity ($V1$–$V5$). Further, the two-layer spiking neural network model was validated by classifying the stimuli based on the CN spike responses (see Results) (Fig. 3D).

2.8. Synaptic seed weights

Pre-synaptic learning, all the excitatory synapses were assigned with randomly generated (normal distribution, $\mu = 0.15$ and $\sigma = 0.15$) initial synaptic weights (Seed Weights, SWs). In this study, we have generated 5 different randomized SW distributions (Figs. 3B, 8A) that further in this text will be referred as "SW_1–SW_5". Additionally, in order to assess the effects of SW generation mechanism, we have tested the synaptic learning rule for SWs generated using both gaussian and log-normal distributions, for varying μ and σ (Figure S4 and S9). The initial inhibitory synaptic weight (w_{inh}) of each synapse was set to 0.2.

2.9. Synaptic weights learning protocol

During synaptic learning phase the CN is fed with PA spike responses for 1500 stimulus presentations in series. Each of this stimulus presentation corresponds to a spatiotemporal pattern of all 96 PA spike inputs (first 1 s of the sliding phase spike responses, Fig. 5). The 1500 presentations were generated from 5 physical stimuli (S1–S5, for a given sensing velocity). Each stimulus presentation was repeated for 300 times. Due to the lack of 300 experimental repetitions of sensory data, we add a gaussian noise ($\mu = 0$ ms and $\sigma = 5$ ms) to each PA spike train (10 experimental repetitions x 30 gaussian repetitions). The gaussian noise addition also helps to attain robust learning. The 1500 stimulus presentations were randomized, to avoid bias in learning from a specific stimulus.

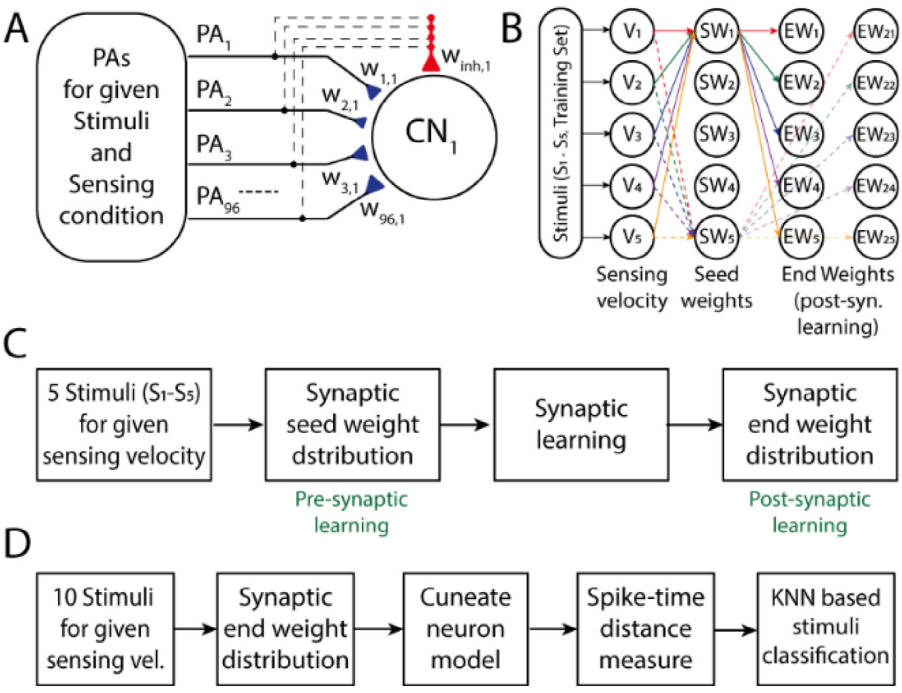

Fig. 3. Synaptic learning protocol. (A) Schematic of network connectivity, where PAs responses are projected onto CN_i as excitatory (blue triangles) and inhibitory synapses (red triangles). (B) The schematic illustration of synaptic learning protocol, through which we achieve 25 different post-training synaptic weight distributions (End Weights, as shown in Figs. 7C, 8B). The variation between each EW configuration, allow each CN to respond for different PA inputs. (C) Simulation flow illustrating the synaptic learning phase. (D) Simulation flow illustrating the testing phase.

2.10. Synaptic learning mechanism

We used calcium-based *'activity dependent synaptic plasticity'* rule in this study. The underlying biological assumptions of this synaptic learning rule, was detailed to cellular level in our previous study (Rongala et al., 2018). Briefly, this synaptic learning paradigm was formulated to potentiate (increase in w_i) the weight of the synapses whose local calcium activity (local calcium, Ca^{2+}_{Loc}) is highly correlated with the total calcium activity of the CN (total calcium, Ca^{2+}_{Tot}) (as illustrated in Fig. 4A). Contrariwise the model depresses a specific synapse (decrease in w_i) whose local calcium activity was de-correlated with the CN total calcium activity.

2.10.1. Excitatory synaptic weight (w_i) learning

Individual excitatory synaptic weights were learnt and updated with each stimulus presentation (see Section 2.9), during the synaptic learning phase. The weight change in each synapse is given by the following equation (illustrated in Fig. 4B–F),

$$\Delta w_i = \int_{t_0}^{t_{max}} \left\{ \left(Ca^{2+}_{Tot}(t) - LPT \right) * Ca^{2+}_{Loc}(t) \right\} * K_i * dt \tag{9}$$

The synaptic weight change (Δw_i), is given by the integral of correlation between the total calcium activity (Ca^{2+}_{Loc}) and local calcium activity (Ca^{2+}_{Loc}), for each stimulus presentation (t_0 to t_{max}). A learning polarity threshold (LPT) was computed in order to regulate the total calcium activity around an equilibrium set point ($SP_{EQ} = 10$). The learning polarity threshold was given by Eq. (10), where the activity gain factor (kw_i) is defined as a function of total excitatory synaptic weight ($\sum w$), with dual slope having zero point preset to SP_{EQ} (slope $= 0.04$, if $\sum w < SP_{EQ}$; slope $= 0.12$, if $\sum w > SP_{EQ}$). The dual slope was adopted in order to avoid rapid potentiation (or) constant depression in synaptic weight, allowing them to regulate around SP_{EQ} (Fig. 4B).

$$LPT = avg\left(Ca^{2+}_{Tot}\right) * kw_i \tag{10}$$

The Ca^{2+}_{Tot} was offset to zero by the LPT, dividing total calcium activity into positive zone (potentiation) and negative zone (depression) (Fig. 4C). Further, the product of total calcium activity and local synaptic calcium activity results in a learning signal (Fig. 4D), who's integral in time (t_0 to t_{max}) would determine if respective synaptic weight is bound towards depression (LTD, negative weight change) or potentiation (LTP, positive weight change) (Fig. 4E). An additional gain factor (k_i, Fig. 4F) was used to define the strength of potentiation and depression for a given synapse. We adapted a sigmoid curve (defined by $S(t) = 1/(1 + e^{-t})$, steepness gain of 0.005) in order to limit the potentiation of a synaptic weight, if its current weight is high (near to 1), and vice versa.

2.10.2. Inhibitory synaptic weight (w_{inh}) learning

The total inhibitory synaptic weight (w_{inh}) was updated for each stimulus presentation (see Section 2.9), during the synaptic learning phase. The w_{inh} was adapted towards an activity set point Ca^{2+}_{SP}, that regulates the calcium firing rate of the CN. An increase in calcium activity in CN will result an increase in the w_{inh} and vice versa. Therefore, the inhibitory synaptic weight was used to keep the calcium firing rate at a predefined *set point* $\left(Ca^{2+}_{SP}\right)$, which was 20 Hz for this simulation. During each stimulus presentation, the inhibitory synaptic weight change (Δw_{inh}) was given by a dual slope function zeroing at the set point $\left(Ca^{2+}_{SP}\right)$. The range of weight change (Δw_{inh}) was set between -0.01 and 0.01 for a calcium spike rate ranging from 0 to 200 Hz. This mechanism results stability in synaptic learning process (excitatory), by avoiding excessive calcium activity or no calcium activity. This synaptic weight adaptation was done based on the average change across last three consecutive learning cycles, in-order to attain a smooth adaptation of synaptic weights.

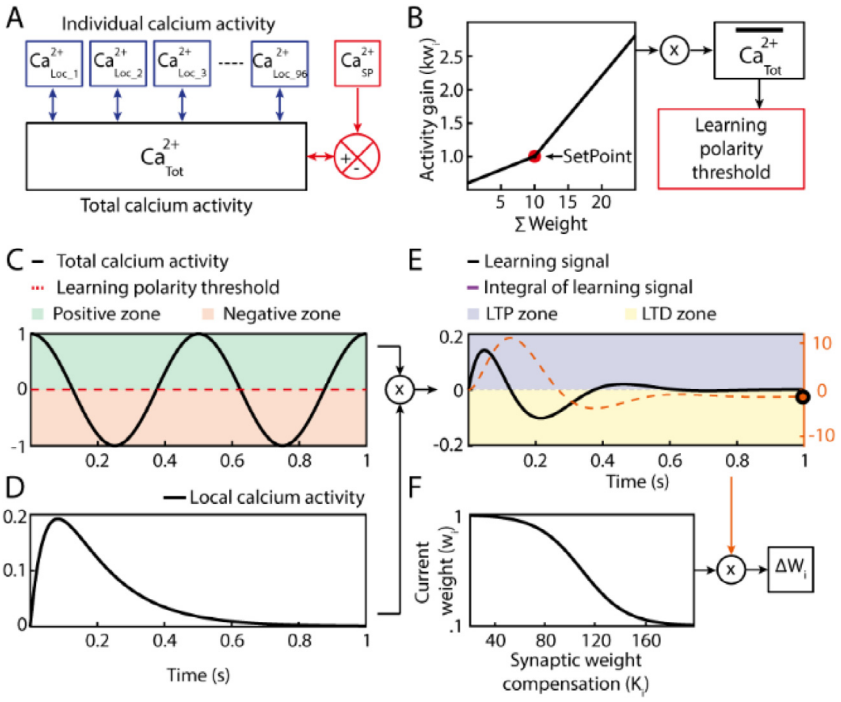

Fig. 4. Synaptic learning mechanism. (A) Schematic illustration of calcium based activity dependent synaptic learning model. (B) Illustration of the 'Learning Polarity Threshold (LPT)' computation. (C) Illustration of total calcium activity in the neuron, which was offset to zero by the LPT, dividing total calcium activity into positive zone (potentiation) and negative zone (depression). (D) The local calcium activity in a single synapse. (E) Learning signal, computed as the product of total calcium activity and local calcium activity. Integral of the learning signal over time. (F) Synaptic weight compensation factor, this is a gain factor that was multiplied with the integral learning signal to calculate the final weight change for that stimulus presentation.

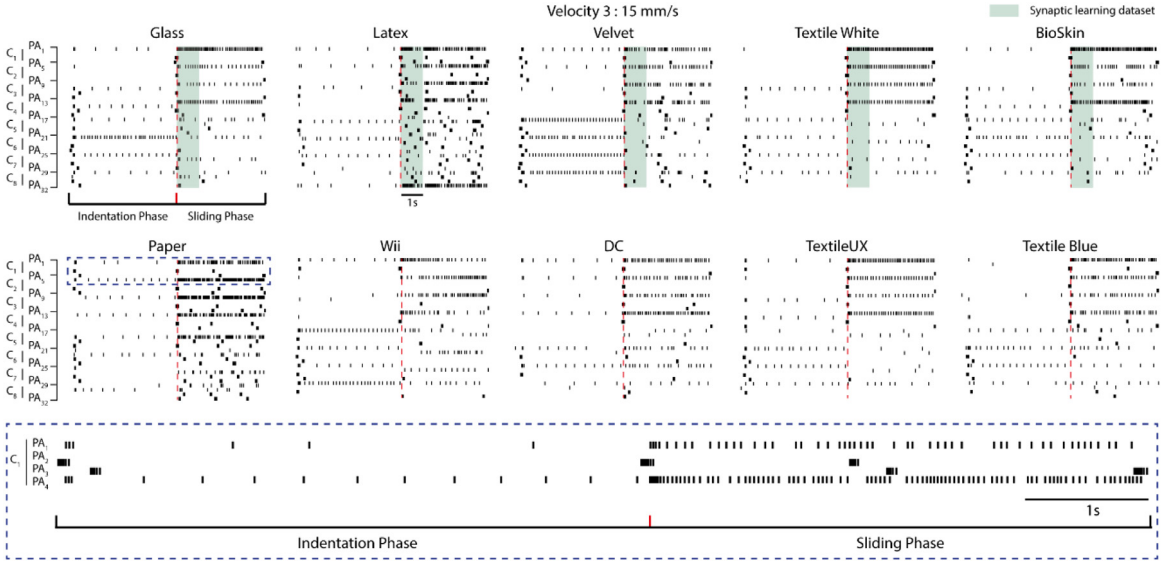

Fig. 5. Primary afferent responses across ten tactile stimuli, for a single sensing velocity. Each row of spike response corresponds to the sensory data as depicted in Fig. 1A (insert). The responses presented here correspond to a sensing velocity of 15 mm/s (V_3), during indentation phase and sliding phase of the experimentation protocol. The green shaded area depicts the dataset chosen for training, i.e. the process of learning the synaptic weights between the PA and the CNs. Inset: Four primary afferent spike responses (PA_1-PA_4) for paper stimuli.

2.11. Data analysis

2.11.1. Multi-Dimensional Scaling (MDS)

We used a classical multi-dimensional scaling method, based on an in-built MATLAB® function "cmdscale". This was used to create a graphical representation (Fig. 7) of excitatory synaptic weight evolution throughout the learning process (for each learning cycle, 1–1500 stimulus presentations, see Section 2.9). Euclidian distance measure was calculated between consecutive learning cycles, across all the PAs. This measure was used as input to represent the change in synaptic weights during learning process across all the PAs.

2.11.2. Victor–Purpura distance

We used Victor–Purpura distance (VPd) measure (Victor & Purpura, 1996) to evaluate the similarities between spike pair

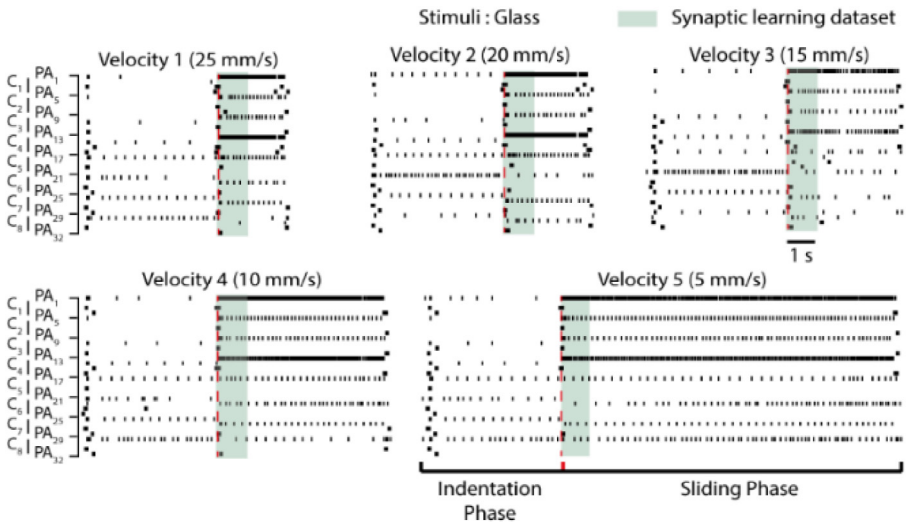

Fig. 6. Primary afferent responses for a single stimulus (glass) across varying sensing velocities (V_1–V_5). Spike responses from each row corresponds to the sensory data as depicted in Fig. 1A (insert). One second data (green shaded area) at start of the sliding phase was chosen for synaptic learning, irrespective of sliding velocity. This allows the synaptic learning to be un-biased of the sensing velocity.

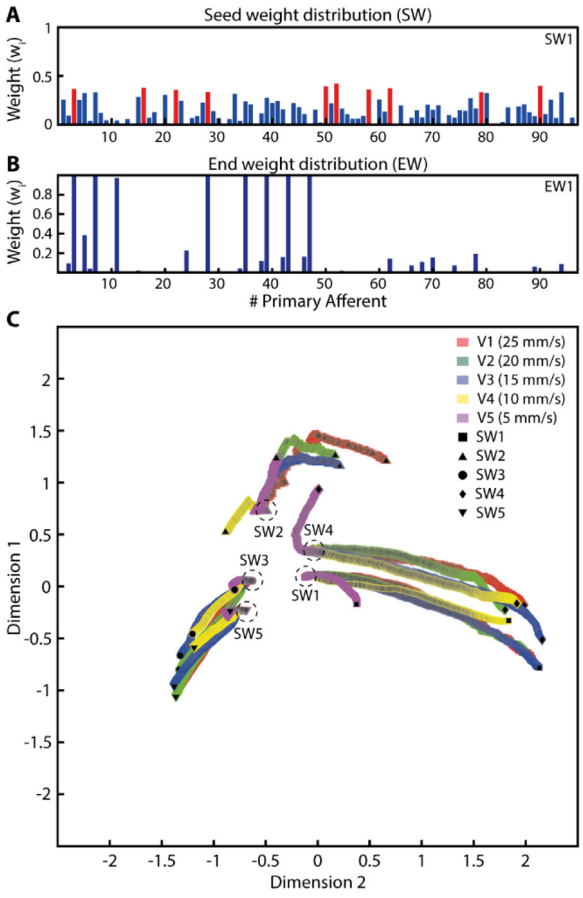

Fig. 7. Synaptic weights. (A) The initial weight (Seed Weight, SW) distribution across all the PA excitatory synapses. (B) The post-training excitatory synaptic weight (End Weight, EW) distribution. (C) Evolution of the excitatory synaptic weights across all the PA synapses, during the synaptic-learning process. A classical multi-dimensional scaling (across Euclidian distance measure) was used to illustrate the divergence in excitatory synaptic weights through learning process (for all the 25 EW configuration, five sensing velocities × five seed weights).

responses. We use this measure to evaluate the information in spike responses of given CNs spike responses (Figs. 9 and 10). This method gives a cost that needed to match two given spike trains. This cost was calculated based on two rules (1) Addition/deletion of individual spikes ($cost = 1$, for each operation). (2) Shifting a spike time for given interval (Δt) ($cost = q.\Delta t$), where q was the gain factor that defines the relevance of time scale for spike trains.

2.11.3. KNN classifier

We constructed a *KNN* classifier to validate the CN spike responses for stimulus decoding (Figs. 11–13), based on VP distance matrix. We have constructed the KNN classifier with 3 neighbors (k = 3), 50% training set and 50% test set. These classes are selected in randomized method. The classifier was run for 100 repetitions and the mean of the decoding percent was reported, this was done in-order to have a vigorous validation across randomly chosen training and test set.

3. Results

3.1. Primary afferent

Contact between tactile sensors and naturalistic textures during a passive touch experimentation protocol (Section 2.3) generated spike responses form first order neurons (or primary afferents (PAs), see Section 2.5). The time-continuous tactile sensor raw data from 8 channels ($C1$–$C8$) were multiplexed into 32 different time-continuous signals using signal processing techniques (see Methods, Section 2.4). These sensory signals were fed as input currents (I_{input}) to a regular spiking Izhikevich neuron model (Izhikevich, 2003), which emulated spatiotemporal spike trains of tactile sensory data. Tactile sensory data was generated for 10 naturalistic textures (tactile stimuli), under five different sensing velocity conditions (V_1–V_5) (25, 20, 15, 10 and 5 mm/s).

In Fig. 5, we display the spike responses of a subset of the PAs ($PA_1 - PA_{32}$) across all tactile stimuli for a single sensing velocity (V_3, 15 mm/s) including both the indentation and the sliding phases of the experimental protocol. For a given stimulus, 8/32 PAs (as PA_3, PA_7 in Fig. 5) exhibit spike bursts during transient-state changes (Fig. 5, *insert*), which imitates the fast adapting (FA) like mechanoreceptor behavior (Abraira & Ginty, 2013; Johansson & Flanagan, 2009). Whereas, 8/32 PAs (as PA_1, PA_5 in Fig. 5)

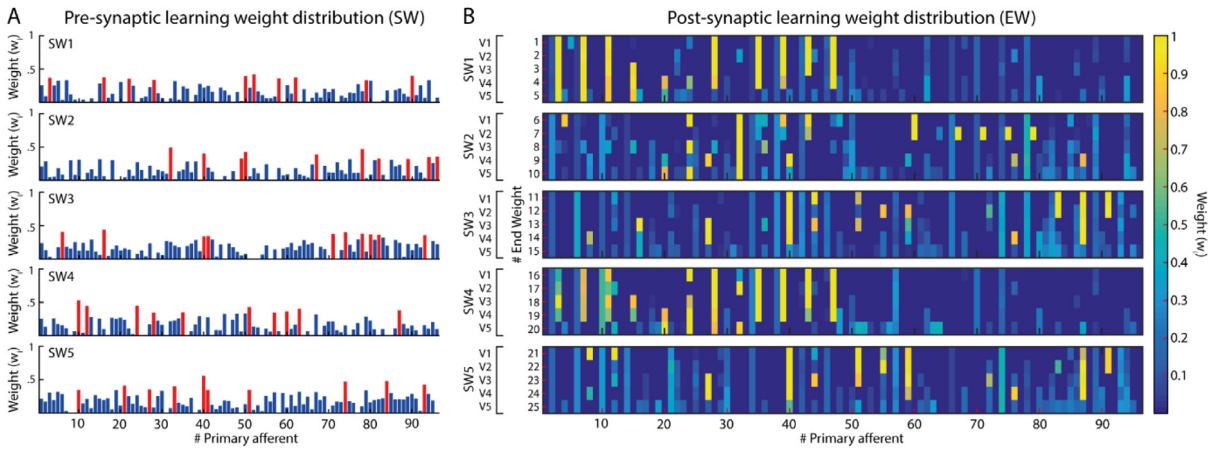

Fig. 8. Excitatory synaptic weight distributions. (A) The five synaptic seed weight distributions, that were generated using random distribution process (mean = 0.15 and $\sigma = 0.15$). (B) The synaptic end weights across PAs, for all 25 EW configurations (as illustrated in Fig. 3E) . (For interpretation of the references to color in this figure legend, the reader is referred to the web version of this article.)

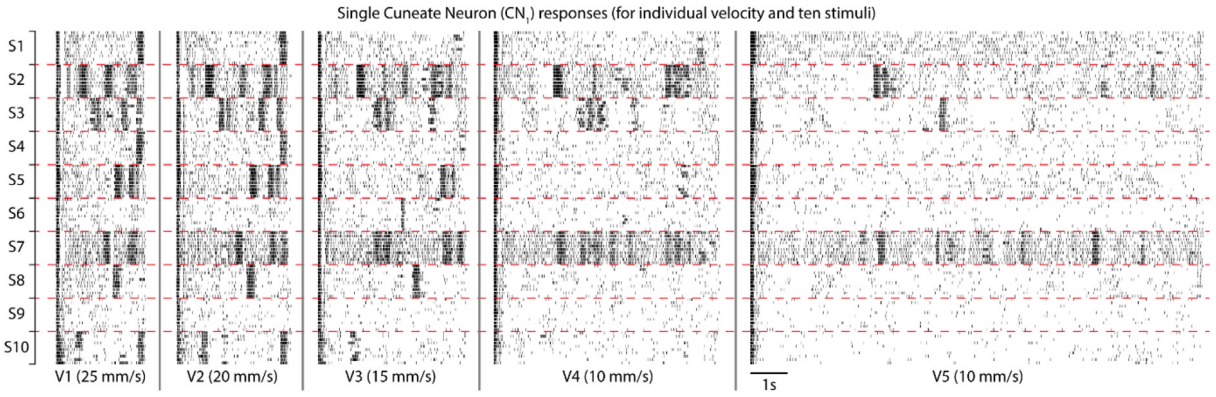

Fig. 9. Single cuneate neuron (CN_1) spike responses. Each column illustrates the spike responses of CN_1 for PA inputs across 10 tactile stimuli (S1–S10, Fig. 1B) and 5 sensing velocities (V_1–V_5). Each stimulus for a given sensing velocity was repeated 10 times experimentally, which were illustrated along rows of the spike responses.

exhibit fast adaptation (with a quick burst) during the start of a transient-state change and further generate more tonic activity in their spiking pattern, imitating the slow adapting (SA) like mechanoreceptor behavior as observed in mammals and humans (Abraira & Ginty, 2013; Johansson & Flanagan, 2009). Different sensory channels exhibit varied spatiotemporal spike patterns (as PA_1, PA_5, PA_9, PA_{13}) creating a rich representation of the input stimulus.

By analyzing the responses at the level of the individual PAs (for example PA_1 in Fig. 5), the temporal spiking pattern varies across all the 10 tactile stimuli (Figure S1A). To quantify the variation in individual spike responses (PA_1, Figure S1A) across stimuli, we clustered them based on two spike train features (spike rate and *ISI-CV*) (Figure S1B). By using a *KNN* classifier (with 5-fold validation) on the clustered PA_1 data, we achieved 94% correct stimulus decoding. This decoding performance in complementary with our previous study (Rongala et al., 2017), affirming that individual PA responses from our adopted neuromorphic implementation, is stimulus specific (during sliding phase).

In order to implement the concept of variable nerve conduction delays from the periphery to the CNs observed in humans and mammals (Johansson & Flanagan, 2009), we have expanded the 32 PA responses (Figs 5, 6) to 96 PA responses by applying two different levels of delays (ΔT = 75, 150 ms) to each of the original PA responses (thus obtaining $PA_{33} - PA_{96}$).

3.1.1. Effect of sensing velocity

In-order to achieve a "Learnt, generalizable representations of the tactile sensing interface", we have explored the effect of the sensing conditions on the synaptic learning algorithm and CN responses. Fig. 6 illustrates the spike responses of PA_1–PA_{32} for a single stimulus (Glass, S1) for 5 different sensing velocities.

At the level of individual PAs (for example PA_1 in Fig. 6), we observe a modulation (along time) of spiking responses inversely proportional to the sensing velocity (as shown in Figure S1C). To study the similarities in PA spike pattern across different sensing velocities, we have normalized the PA_1 responses in space (Figure S1D). The PA spike times are normalized based on prior knowledge of sensing velocity. The space normalized PA_1 responses were convolved (Figure S1E) with an exponential decay ($\tau = 2$ mm), and the similarity between these convoluted signals was evaluated using cross-correlation measure (with zero-lag). The cross-correlation coefficient across all convolved signals resulted between 0.96 $\sim$ 0.99 (Figure S1F). This implies that temporal firing patterns of the spike responses were similar irrespective of sensing velocity. This result suggests that PA spike responses might carry information about the spatial structure of the stimulus (irrespective of the sensing velocity), forming a basis for generalized stimulus decoding (irrespective of sensing velocity, Section 3.3.4).

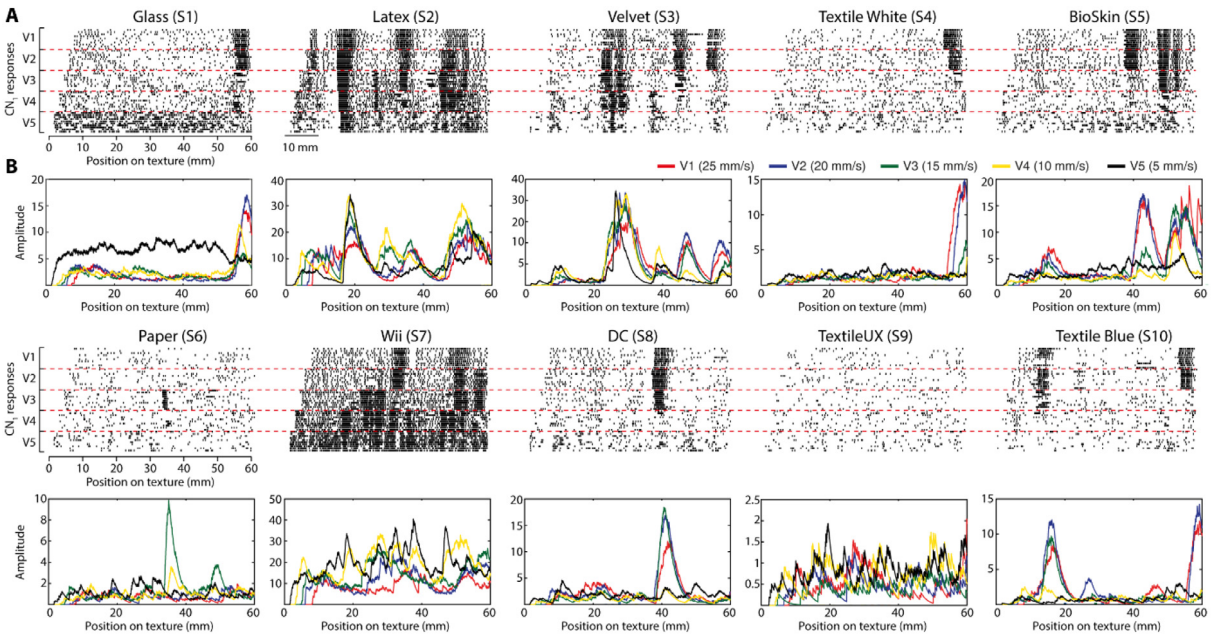

Fig. 10. Normalized cuneate neuron (CN_1) responses. (A) The CN_1 responses (shown in Fig. 9), were normalized on space (relative position of the tactile sensor on stimulus). (B) Convolution of the normalized CN_1 spike responses, with an exponential decay ($\tau = 2$ mm). Each signal displayed, was the mean across 10 experimental repetitions.

3.2. Synaptic learning

All the 96 PA responses ($PA_1 - PA_{96}$), were provided to cuneate neurons (CNs) as excitatory and inhibitory synaptic weights (w_i, w_{inh}) (Fig. 3A). Pre-synaptic learning, the excitatory weights were defined as normal distribution (Seed weights (SWs), Section 2.8 and Fig. 7A). Following a synaptic learning protocol (Section 2.9), i.e. a time series of tactile sensing conditions and the gradual synaptic weight transformations imposed by the synaptic learning model (Section 2.10), the synaptic weights acquired a post-learning synaptic weight distribution (End Weights (EWs), Fig. 7B). The normal distribution of SWs (Figure S2, 7A) evolved into a bi-modal EW distribution (Figure S2, 7B), post-learning. Similar phenomenon of few high EWs was previously observed in the CN *in vivo* recordings (Bengtsson et al., 2013; Jörntell et al., 2014).

The synaptic learning had resulted in dimensionality reduction based on specific input tactile features, that had constituted for information maximization. This was validated based on stimulus decoding performance of CN spike responses (post-synaptic learning, using EWs). We used Victor–Purpura spike distance measure along with *KNN* classifier to perform the stimulus decoding (detailed in Section 2.11). Based on the spike responses of a single CN with synaptic SW ($SW1$) distribution (Figure S3A), we achieved a stimulus decoding performance between 11.76%∼62.14% (across 5 sensing velocities). Whereas, from the responses of the same CN with EW (EW1) distribution (Fig. 10), we were able to achieve a decoding performance between 51.76%∼83.62% (Figure S3B, C).

Based on a previous study (Rongala et al., 2018), the chosen synaptic learning rule was established to award the PA synapses that are in high correlation. Therefore, the learning rule potentiates (increase) PA synapses that exhibit synchronized firing behavior with the PA that has high initial SW (red bars in Fig. 8A). This makes the SW distribution an important component of synaptic learning. We have used a multi-dimensional scaling (MDS) method (Section 2.11.1), to visualize the synaptic weight changes from SW to EW as shown in Fig. 7C. From this analysis, it is evident that the synaptic EWs take a different direction (relative to each other) based on their initial weight distribution ($SW1$–5, Fig. 8A).

To assess the effects of seed weight generation mechanism, we have tested the synaptic learning rule for SWs generated using both gaussian and log-normal distributions, for varying mean (μ) and standard deviation (σ) (Figures S4 and S7). For gaussian distribution, we tested the learning algorithm for each combination of μ and σ between 0.05 to 0.25, with step of 0.05. Whereas, for log-normal distribution we have tested the learning algorithm for each combination of μ and σ between 0.6 to 1, with step of 0.1.

With variation in gaussian distribution parameters, we noticed for smaller σ ($\sigma = 0.05$ and 0.10) there is higher degree of variation from SW to EW landscape ("weight landscape" denotes the distribution of weights across all the 96 PA synapses) (Figures S4 and S7). From Figure S4, we notice that SWs with low μ and σ (μ and $\sigma < 0.10$) tend to have a clear bimodal EW distribution. Whereas, SWs with high μ and σ (μ and $\sigma > 0.20$) have difficulties in resulting higher EWs. We have performed stimulus decoding (using VPd and *KNN*, see Section 2.11) based on the spike responses of CN with these EWs (corresponding to the SWs and EWs in Figure S4) to realize the effect of variation in gaussian distribution parameters. We achieved a stimulus decoding percentage ranging between 79.46% to 98.6%, with a mean decoding of 89.34% (Figure S6). Further, by considering log-normal SW distribution (Figure S7), we found that the learning algorithm tends to achieve a bi-modal EW distribution even for variation in the distribution parameters (μ and σ). We achieved a stimulus decoding percentage ranging between 79.06% to 89.36%, with a mean decoding of 82.14% (Figure S9) based on CN response for the EWs learnt using log-normal SW distribution. These results indicate that the proposed learning algorithm is robust to the variation in SW generation mechanisms.

We have simulated synaptic learning for a configuration of five different SW distributions (Fig. 8A) and PA responses for five different sensing velocities, which resulted in 25 varied EW distributions (see Section 2.7 and Fig. 8B). During synaptic learning phase, only the first 1 s data of PA responses during the sliding phase (shaded zone in Figs. 5, 6) was considered as input to the

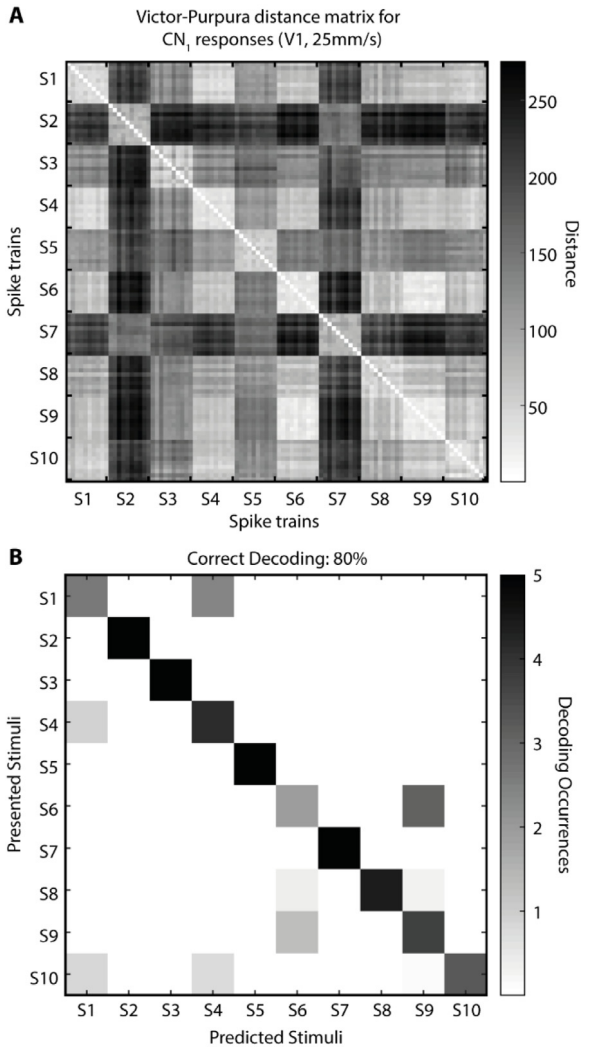

Fig. 11. Stimulus decoding across single cuneate neuron (CN_1) responses, for PA inputs of single sensing velocity (V_1). (A) Victor–Purpura distance measure was used to evaluate the dissimilarities between the stimulus spike responses of CN_1 (Fig. 9, first column data). The VP_d cost $q = 10$/s. (B) Confusion matrix based on *KNN* classifier, with 50% training set, 50% test set and $K = 3$. Using this classifier, we achieved a correct stimulus decoding performance of 80%.

learning algorithm. This was done in order to avoid the bias of sensing velocity on the synaptic learning algorithm. However, post-synaptic learning, the proposed algorithm was able to pick similar high EWs for a given SW distribution and varying sensing velocities (Figs. 7C, 8). This strengthens the goal of forming generalized tactile feature representation.

3.3. Cuneate neurons

In order to validate the two-layer spiking neural network and assess the generalization capabilities of such network, we opted to perform stimulus classification based on the CN responses. Post-synaptic learning we achieve 25 varied end weight distributions (Fig. 8). Each synaptic end weight (EW) distribution allows a unique combination of PA inputs to be relayed onto CN, leading to a distinctive CN responses. Therefore, further in this article CNs labeled CN_1–CN_{25} indicate the second order neuron model responses, for respective synaptic end weight configuration (EW_1–EW_{25}).

3.3.1. Single cuneate neuron responses

In this section we analyze individual cuneate neuron responses for PA inputs corresponding to all 10 tactile stimuli (S_1–S_{10}) under five sensing velocities (V_1–V_5). In Fig. 9, we show CN_1 (based on EW_1) spike responses resulting to PA inputs for all 10 stimuli and 5 sensing velocities. The spike trains were shown in a matrix structure, where rows display spike responses across stimuli (separated with red dotted lines) and columns display spike responses with respect to the sensing velocity. The 10 rows of spiking responses (for every given stimulus and sensing velocity), indicate the experimental repetitions from passive touch experimental protocol (Section 2.3). The experimental repetitions were carried out to assess repeatability of the system presented in this study (Fig. 9). To evaluate this repeatability in presented neuron model responses, we convolved the CN_1 spike responses with an exponential decay ($\tau = 0.5$ s) and performed cross-correlation measure across all the experimental repetitions (for each stimulus and sensing velocity). This analysis yielded an average cross-correlation coefficient of 0.84, signifying robustness of our two-layer spiking neural network model across experimental repetitions.

From the CN_1 responses shown in Fig. 9, it can be perceived that the spatial pattern of each stimulus was preserved irrespective of sensing velocity. In order to qualitatively evaluate this claim, we have normalized the CN_1 spike responses in space, based on the prior knowledge of sensing velocity (Fig. 10A). The normalized CN_1 spike responses were convolved using an exponential decay ($\tau = 2$ mm) (Fig. 10B). A cross-correlation measure (with zero-lag) was performed to determine similarities in these convolved signals. For all 10 stimuli, we achieved an average cross-correlation coefficient between 0.65∼0.91 (i.e. 0 indicating high dissimilarity, and 1 indicating high similarity) across convolved signals from different sensing velocities (Figure S10). Whereas, the cross-correlation coefficient was low (<0.5) for some CN_1 responses based on low sensing velocities (V_4 *and* V_5, 10 and 5 mm/s), for certain stimuli ($S_1, S_4, S_5, S_8, S_{10}$), which could be a result of the stimulus surface property (see discussion).

Overall, with a notable cross-correlation measure across CN_1 responses for varied sensing velocities (Figure S10), paved strong ground towards generalized stimulus decoding.

3.3.2. Validation of single cuneate neuron responses

To evaluate CN spike responses, we have performed stimulus decoding. We adopted Victor–Purpura (Victor & Purpura, 1996) spike distance measure, that determine the similarity between two given spike trains for a pre-defined time shift cost q (see Section 2.11.2). Lower the Victor–Purpura distance (VP_d) measure, more similar the spike trains and vice-versa. As part of initial validation, we performed the stimulus decoding based on CN spike responses for PA inputs corresponding to single sensing velocity (V_1, 25 mm/s). We performed VP_d measure ($q = 10$/s) between each spike pair of CN_1 responses (Fig. 9), for 100 sets of PA inputs (10 stimuli x 10 experimental repetitions). The *VP* distance matrix for this computation was shown in Fig. 11A. Each stimulus was arranged in blocks of 10 repetitions. Based on this distance measure, we built a *KNN* classifier to validate the CN_1 responses. A correct decoding performance of 80% was achieved with 50% training set, 50% test set and $K = 3$ (Fig. 11B).

We further extended our analysis to validate all 25 CNs, for PA inputs corresponding to individual sensing velocity. We have computed *VP* based distance matrix (as mentioned above) for individual CN (1–25) responses, for 100 sets of PA inputs (10 stimuli x 10 experimental repetitions, for a given sensing velocity (V_1–V_5)). Using a *KNN* classifier (50% training set, 50% test set, $K = 3$), we achieved a stimulus decoding performance ranging between 32.1%∼94.2% across all 25 CN responses, for PA inputs

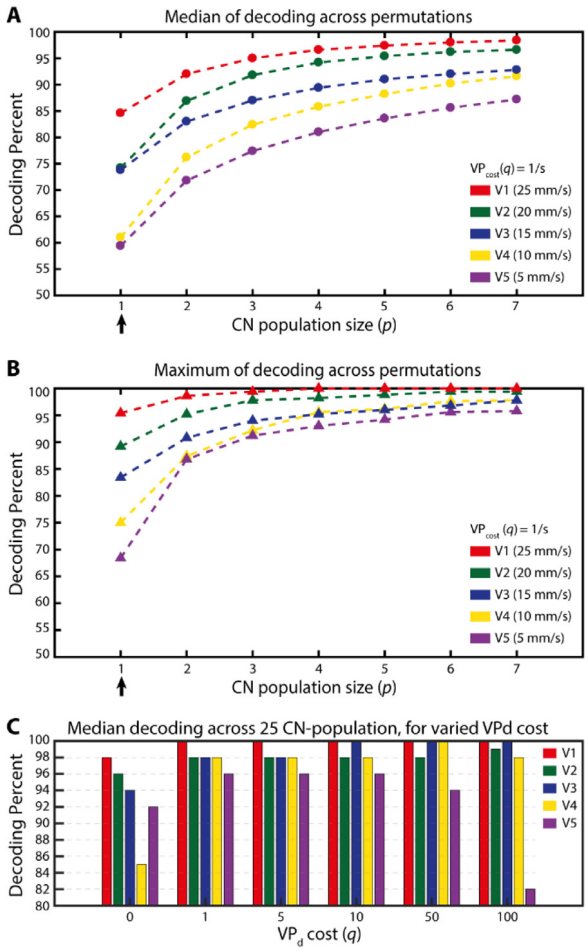

Fig. 12. Stimulus decoding across pairs of CNs, for individual sensing velocities. (A) Victor–purpura distance-based stimulus decoding was carried out across individual CN responses (q = 1/s). The median of decoding percent across all possible n-combinations for a CN population size was presented. (B) Maximum decoding percent across all the possible n-combinations for a CN population size. (C) Median decoding percent across all the 25 CNs, for varied VP_d cost.

based on given sensing velocity (Figure S11). On an average across all the 25 CNs, the stimulus decoding performances were 84.66%, 77.24%, 74.78%, 62.30% and 48.61% for respective sensing velocity V_1, V_2, V_3, V_4 *and* V_5 based PA inputs. This analysis present a clear effect of sensing velocity on the stimulus decoding performance.

3.3.3. Validation across population of cuneate neurons responses

We performed stimulus decoding procedure by grouping the response from n CNs. For this analysis, we formed different sets composed increasing number of CNs (p, Fig. 12A, B). In a given set of population size p and total number of neurons n (= 25), the number of all possible combinations (^nC_p) are considered $\left({}^nC_p = n!/((n-p)!p!)\right)$. In this section, we consider the CN responses based on the PA inputs for individual sensing velocities.

The maximum stimulus decoding performance was computed (using *KNN* classifier based on VP_d measure (q = 1/s)) across all the CNs responses for the given combination set. Further, we compile the median and maximum of decoding percent across all the possible CN combinations in a set (Fig. 12A, B). Comparing the decoding performance between individual CNs and pairs of CNs (p = 2), we found a significant increase in stimulus decoding performance between 3.2% to 18.4% with a mean increase of 10.2% (Fig. 12A, B). Considering pairs of 2 CNs (p = 2), the median of stimulus decoding performance ranged between 70%∼90% across all 5 sensing velocities and the maximum stimulus decoding performance was between 68%∼95%. Whereas, considering bigger CN pair size (p = 5) the stimulus decoding percentages significantly increased to 80%∼96% (median) and 90%∼100% (maximum). When all the 25 CNs (p = 25) were considered, we achieved a median stimulus decoding percent of 82%∼100% (and maximum decoding percent of 95%∼100%) for individual sensing velocity based PA inputs (Fig. 12C). We also investigated the stimulus decoding performance as a function of varying VP_d cost (q) in-order to assess the robustness of this measure (q, Fig. 12C). The stimulus decoding performance remained firm between 90% ∼ 100% (except in one condition where q = 100 and at a low sensing velocity V_5) across all the given sensing velocities for changing VP_d cost (q = 1 ∼ 100). The decoding performance for q = 0, corresponds to the spike rate of CN responses.

3.3.4. Validation across population of cuneate neurons responses (generalization)

In above sections, we have validated the stimulus decoding performance based on individual CN responses and pairs of CN responses, for PA inputs based on individual sensing conditions. In this section we analyze and validate the CN responses based on PA inputs irrespective of sensing velocity. Due to difference in length of spike trains for varied input sensing velocities, we normalized the CN responses on space based on prior knowledge of the sensing velocity (as spike responses shown in Fig. 10A).

We have determined spatial Victor–Purpura distance measure (sVP_d), where the *VP* cost (q) for time shifting spikes was replaced by space-shifting cost (q_s, see Section 2.11.2). This adaptation of VP helped in assessing the spike trains that were normalized in space (Fig. 10A). We computed *sVP* distance matrix for individual CN (CN_1–CN_{25}) responses for PA inputs across all 10 stimuli and all 5 sensing velocities. We grouped individual cuneate neuron responses based on stimulus (irrespective to the sensing velocity). We performed stimulus decoding across individual CN responses using *KNN* classifier (with 70% training set, 30% test set, K = 5). The maximum stimulus decoding performance across all the 25 CNs was reported in Fig. 13 (red line with circle marker). Irrespective of sensing velocity we achieved a strong stimulus decoding performance of 96% ($q_s = 0.5$).

Crucially, in order to assess the generalizability of the information content in CNs, we have modified the *KNN* classifier. We have removed the sVP_d data that corresponds to two sensing velocities (V_2 *and* V_4) from the training set of *KNN* classifier. Whereas, the classifier test set contains sVP_d data for all five sensing velocities. By performing such procedure, we assess if the classifier could identify stimulus, from the responses that were never experienced before by the classifier. The decoding performance results from this classification technique was labeled as "generalized classifier" in Fig. 13 (blue line with triangle marker) and rest of this article. Based on this classification technique, we yielded a stimulus decoding percent of 94.5% (*for* $q_s = 0.5$) which establishes the generalizable capabilities of the two-layer spiking neural networks and adopted synaptic learning techniques in this research study.

We have also tested the generalized stimulus decoding across different sVP_d cost (q_s) in Fig. 13. We achieved a strong classification until certain VP_d cost ($q_s = 7.5$), further the performance decreases as a result of loss in spatio-temporal information after a certain spike shifting cost.

4. Discussion and conclusion

The main objective of this study has been to construct a neuromorphic tactile system, that could learn and represent input

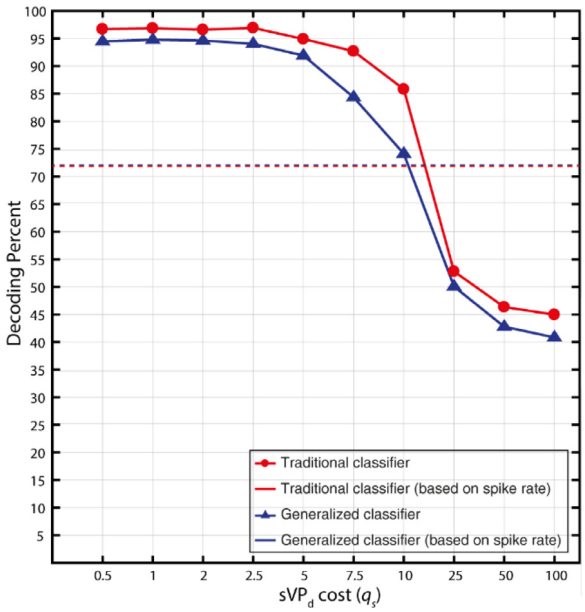

Fig. 13. Stimulus decoding across all 25 CN responses that were normalized on space. The normalized responses of individual CNs are paired according to stimulus irrespective of their velocity. A *KNN* classifier with 70% training set, 30% test set and $K = 5$ was adopted to define stimulus decoding percentage across each individual CN. Further, maximum decoding percent across all 25 CN was reported in this plot. Traditional classifier: all 5 sensing velocities (V_1–V_5) based stimulus responses are considered in both training and test set of the KNN classifier. Generalized classifier: only three velocities (V_1, V_3 and V_5) based stimulus responses are considered in training set, and all the five velocity-based responses are used in the test set of the KNN classifier.

tactile features under generalized sensing condition. Towards this objective we have developed a bio-mimetic functional tactile system based on neuro-inspired computational models and learning algorithms. This system was successful in differentiating naturalistic textures (trained and un-trained) under varying sensing conditions.

A bionic fingertip-like tactile sensor was used to explore naturalistic textures under passive touch protocol by means of a mechatronic platform (Fig. 1A, B, C). Further, an Izhikevich neuron model was adopted to encode mechanoreceptor-like (Primary Afferent, PA) spike responses from the tactile sensory data. This neuromorphic adaptation was proven to be stimulus specific (a stimulus decoding accuracy of 95%, Figure S1) and robust from our previous studies (Oddo et al., 2016; Rongala et al., 2017; Spigler, Oddo, & Carrozza, 2012), and also in this current work (Figure S1). These studies were based on individual channel sensory data. Whereas, the human hand was approximated to have 10 000 s of PAs spread across a hand (Johansson & Flanagan, 2009), with hundreds of PAs projecting onto a single cuneate neuron (2nd order neurons). There is no existing biomimetic tactile system that can imitate a sensory population to that extent or neither even in a small population of 100 sensory channels (Yi, Zhang, & Peters, 2018; Yousef, Boukallel, & Althoefer, 2011). To tackle this challenge, in this study we have pre-processed the sensory data to multiplex 8 active sensory channel (physical sensors) data to 32 sensory signals (see Methods, Fig. 1A *insert*). Addition to this sensory processing we have added two conduction delays to all the sensory signals. This was done with a motive to replicate the nerve conduction delays as observed in humans and mammals (Johansson & Flanagan, 2009). In field of neuroscience, the role of conduction delays was only hypothesized, but there was no clear validation of its advantage in processing tactile information. However, implementing these delays mechanisms for tactile information processing in robotics has been proved advantageous for extracting certain haptic features (Bologna et al., 2013; Rongala et al., 2019). Such sensory data elaborations are essential for synaptic learning algorithm to extract varied haptic features. Based on these signal processing techniques and fine-tuned Izhikevich neuron parameters, we were able to recreate various firing dynamics properties that resemble slow and fast adapting mechanoreceptors-like responses (Figs. 5, 6). Additionally, in order to validate the generalized sensing capabilities we explored each tactile stimulus under five varying sensing velocities (5, 10, 15, 20, 25 mm/s). We realized for a given stimulus the firing pattern of PA spike responses were consistent across different sensing velocities (a cross-correlation of 0.96∼0.99, Figure S1C, D, E, F). This lay strong ground to our objective of learning and representing tactile features in generalized sensing conditions.

We adapted a calcium based cuneate neuron model and synaptic learning rule, that were modeled based on the intracellular dynamics as observed in cuneate neuron *in vivo* recordings (Rongala et al., 2018). In previous biological studies conducted on cuneate neurons in adult mammals (Bengtsson et al., 2013), it was observed that these neurons exhibit strong bi-modal synaptic weight distribution with few high synaptic weights and other very low synaptic weights (silent synapses). Such phenomenon was dubbed to act as feature extractor, by reducing high-dimensional sensory inputs to a few important learnt dimensions (Jörntell et al., 2014). Therefore, we designed a calcium activity dependent synaptic plasticity rule based on multiple assumptions and *in vivo* recordings (Rongala et al., 2018). We implemented the cuneate nucleus as a feedforward network with homeostatic plasticity rule (self-stabilizing learning mechanism). A similar structure was proposed in Kasabov (2010). However, in Kasabov (2010) the plasticity is supervised while that was based only on the current internal state of the neuron and not on classification results. Overall, Kasabov (2010) mimics more closely higher level/abstract processes of classification, while our model was more grounded into the dynamics of peripheral nervous system as needed for our neuroprsothetic purposes.

This learning rule was established to learn the sensory correlations from input PAs synapses. Based on such learning rule, by assigning randomly distributed initial synaptic weights (presynaptic learning, 'seed weights (SWs)') we allow the learning algorithm to pick correlation in the input sensory synapses with respect to the random combination of high initial synaptic weights. Therefore, leading to pick a set of synapses that were responding to a specific haptic feature in the input sensory space. This results in few highly correlated synapses to have high weights post-synaptic learning (end weights (EWs)). Hence, different SWs distribution would allow the algorithm to pick different haptic features (from resulting EWs) in the input sensory space. In the current study we were able to reproduce such phenomenon (Figs. 7, 8). The learning algorithm was validated by stimulus decoding performance, which raised from 11.76%∼62.14% (with synaptic SW distribution) to 51.76%∼83.62% (with synaptic EW distribution) (see Section 3.2, Figure S3). Further, we studied the effect of seed weight generation mechanism on the learning algorithm (Section 3.2, Figures S4–S11). We found that our learning algorithm is sensitive to the variation of synaptic SW distribution parameters (mean (μ) and standard deviation (α)), where in some cases of high μ and α the learning mechanism finds hard to have high end weights (or bimodal distribution). However, the synaptic learning algorithm still tries to segregate EWs from SWs for any given μ and σ. This can be perceived from a high stimulus decoding percentage ranging between 79.46% to 98.6% with a mean decoding of 89.34% (Figure S6), for gaussian SW distribution, and stimulus decoding percentage ranging between

79.06% to 89.36% with a mean decoding of 82.14% (Figure S9), for log-normal SW distribution.

Crucially, we found that the synaptic EWs based on PA inputs associate with different sensing velocities but same SW, evolve to have similar high-EW synapses (Figs 7C, 8B). This further strengthens the generalization in input feature learning, irrespective of sensing velocity.

In order to validate the two-layer spiking neural network and assess the generalization capabilities of such network, we opted to perform stimulus classification based on the CN responses. We have trained 25 CNs based on the combination of 5 different SW distributions (SW1-5) and PA inputs for 5 different sensing velocities (see Sections 2.7 and 3.2). Further we performed stimulus classification on CN responses (Fig. 9) using Victor–Purpura spike train measure. This resulted in an average correct decoding percent of 84.66% (min: 76.1%, max: 94.3%) across all the 25 CNs individually, for PA inputs associated to single sensing velocity (V_1, 25 mm/s) (Fig. 11, S5). Further, we achieved decoding performance between 32.1%∼94.2% across all individual CNs for PA inputs with varied sensing velocities (Figure S11). We found that the decoding performance consistently worsens along with reduced sliding velocity, mostly for the two lower velocities (V_4 *and* V_5, 10 and 5 mm/s). The effect of slow sliding velocity was already evident (cross-correlation coefficient <0.5) in PA responses (Figure S10). This could be a result of force-based control strategy used in the mechatronic platform (Oddo, Beccai et al., 2011; Oddo, Controzzi et al., 2011), where the stimuli were slid (using a voice coil, with absolute tracking error $<$ 20 mN) along the surface of the tactile sensor with a pre-defined contact force (400 mN). With slow sliding velocity the voice coil adapts its height in order to maintain the intended contact force between the stimuli and tactile sensor, indirectly results in adapting to the irregularities in stimuli surface and subsequently losing some temporal properties.

Further, we performed stimulus decoding across an ensemble of CN networks responses for PA inputs corresponding to individual sensing velocity. An average decoding performance over all the possible combination of 25 CNs, for a specified size of CN population was considered (Section 3.3.3). Through this co-operative decoding methodology, we voted for maximum and median decoding performance across the CN population (p) (Fig. 12A, B). The decoding performance has increased from 59.4%∼84.6% (median voting, $p = 1$) to 82%∼100% (median voting, $p = 25$) (Fig. 12C). This high decoding performance shows the significant amount of stimulus specific features encoded by our two-layer network.

Lastly, we opted to validate generalized stimulus decoding (decoding stimulus irrespective of sensing velocity) based on all 25 CNs responses. In humans we have multiple sensory perceptions, where fusion of these sensory data can construct a multi-dimensional sensory perception. For example, during a tactile manipulation task, sensory data from skin stretches, muscle movements contribute to a proprioceptory feedback, assisting us to estimate the sensing velocity. On basis of which we could normalize the tactile sensory data. In our modeling approach to perform generalized decoding, we normalized the CN spike responses across space (with prior knowledge of velocity). As a first step, we analyzed a single CN responses (normalized in space) for each stimulus across PA inputs based on different sensing velocity (Fig. 10). We found the firing pattern of CNs responses remain certain (average cross-correlation coefficient between 0.65∼0.91, across all stimuli), for varying sensing velocities (Figure S10). Based on this verification, we performed stimulus decoding across normalized CNs responses using spatial Victor–Purpura measure and KNN classifier (test set = 70%, training set = 30%, $K = 5$). From which, we have achieved a maximum decoding performance of 96% across all 25 CNs (for cost $q_s = 0.5$, Fig. 13). In order to also generalize the classification method, we have trained the *KNN* classifier with CN responses associated to only PA inputs (for all 10 stimuli) from three sensing velocities (V_1, V_3 *and* V_5). Further, tested the classifier with PA inputs (for all 10 stimuli) for all five sensing velocities ('Generalized classifier'). This procedure yielded a decoding performance of 94.5% (for cost $q_s = 0.5$, Fig. 13). The high stimulus decoding performance across CNs responses irrespective of varying sensing velocities confirms that our system could learn and represent input tactile features under generalized sensing condition.

With the learning model presented in this article, we were able to create a representation free feature extractor. Any artificial neural networks can be added on top of the presented model to learn and classify the input stimuli. The learning mechanism proposed in this study can also be used to address the problem of initial weight configuration in artificial neural networks (Glorot & Bengio, 2010; He, Zhang, Ren, & Sun, 2015). With neuronal regulatory mechanisms and self-stabilizing learning, we were able to create a bio-inspired feature extractor with generalized learning capabilities. This system can be reliable for robotic applications but could be potentially expanded to other application domains ranging from bionics up to climate data as approached by prior art (Kasabov et al., 2016).

In this research study, we found implementing SNN with a realistic calcium plasticity model, can be efficient in learning the emergent features in the temporal evolution of a 2D space, and performing an accurate classification. The adopted learning rule reinforces the correlations present in the random seed weights, which at the same time ensures robust feature extraction and makes each cuneate neuron unique potentiating population encoding. Interestingly, these results are achieved with a large fraction of silent synapses, which at the same time might be energetically efficient and can allow mimicking the actual neurophysiology of the cuneate nucleus.

Acknowledgments

This work was supported in part by the Ministry of Education, Universities and Research of the Italian Republic and the Swedish Research Council, via the Italy–Sweden bilateral Research Project J52I15000030005 SensBrain (Brain Network Mechanisms for Integration of Natural Tactile Input Patterns); in part by EU Grant FET 611687 NEBIAS Project (NEurocontrolled BIdirectional Artificial upper limb and hand prosthesiS); in part by EU Grant FP7-NMP 228844 NANOBIOTOUCH project (Nanoresolved Multi-Scan Investigations of Human Tactile Sensations and Tissue Engineered Nanobiosensors); in part by the Dubai Future Foundation through Guaana.com open research platform; in part by the Italian Ministry of Education, Universities and Research within the "Smart Cities and Social Innovation Under 30" program through the PARLOMA Project (SIN_00132); and in part by the EU Grant FET 829186 ph-coding (Predictive Haptic COding Devices In Next Generation interfaces).

Appendix A. Supplementary data

Supplementary material related to this article can be found online at https://doi.org/10.1016/j.neunet.2019.11.020.

References

Abraira, V. E., & Ginty, D. D. (2013). The sensory neurons of touch. *Neuron*, *79*(4), 618–639. http://dx.doi.org/10.1016/j.neuron.2013.07.051.

Bengtsson, F., Brasselet, R., Johansson, R. S., Arleo, A., & Jörntell, H. (2013). Integration of sensory quanta in cuneate nucleus neurons in vivo. *PLoS One*, http://dx.doi.org/10.1371/journal.pone.0056630.

Bensmaia, S. J., Denchev, P. V., Dammann, J. F., Craig, J. C., & Hsiao, S. S. (2008). The representation of stimulus orientation in the early stages of somatosensory processing. *Journal of Neuroscience*, *28*(3), 776–786. http://dx.doi.org/10.1523/JNEUROSCI.4162-07.2008.

Bologna, L. L., Pinoteau, J., Passot, J. B., Garrido, J. A., Vogel, J., Vidal, E. R., et al. (2013). A closed-loop neurobotic system for fine touch sensing. *Journal of Neural Engineering*, *10*(4), 046019. http://dx.doi.org/10.1088/1741-2560/10/4/046019.

Brette, R., & Gerstner, W. (2005). Adaptive exponential integrate-and-fire model as an effective description of neuronal activity. *Journal of Neurophysiology*, http://dx.doi.org/10.1152/jn.00686.2005.

Chou, T. S., Bucci, L. D., & Krichmar, J. L. (2015). Learning touch preferences with a tactile robot using dopamine modulated STDP in a model of insular cortex. *Frontiers in Neurorobotics*, http://dx.doi.org/10.3389/fnbot.2015.00006.

Dario, P., Carrozza, M. C., Guglielmelli, E., Laschi, C., Menciassi, A., Micera, S., et al. (2005). Robotics as a future and emerging technology: Biomimetics, cybernetics, and neuro-robotics in european projects. *IEEE Robotics & Automation Magazine*, http://dx.doi.org/10.1109/MRA.2005.1458320.

Fourcaud-Trocmé, N., Hansel, D., van Vreeswijk, C., & Brunel, N. (2003). How spike generation mechanisms determine the neuronal response to fluctuating inputs. *The Journal of Neuroscience : The Official Journal of the Society for Neuroscience*, http://dx.doi.org/10.1523/JNEUROSCI.23-37-11628.2003.

Friedl, K. E., Voelker, A. R., Peer, A., & Eliasmith, C. (2016). Human-inspired neurorobotic system for classifying surface textures by touch. *IEEE Robotics and Automation Letters*, http://dx.doi.org/10.1109/lra.2016.2517213.

Genna, C., Oddo, C. M., Wahlbom, A., Mazzoni, A., Micera, S., & Jörntell, H. (2018). Bilateral tactile input patterns decoded at comparable levels but different time scales in neocortical neurons. *The Journal of Neuroscience*, http://dx.doi.org/10.1523/jneurosci.2891-17.2018.

Glorot, X., & Bengio, Y. (2010). Understanding the difficulty of training deep feedforward neural networks. *Journal of Machine Learning Research (JMLR)*.

Hay, E., & Pruszynski, J. A. (2018). Synaptic integration across first-order tactile neurons can discriminate edge orientations with high acuity and speed. *BioRxiv*, http://dx.doi.org/10.1101/396705.

He, K., Zhang, X., Ren, S., & Sun, J. (2015). Delving deep into rectifiers: Surpassing human-level performance on imagenet classification. In *Proceedings of the IEEE international conference on computer vision* http://dx.doi.org/10.1109/ICCV.2015.123.

Huguenard, J. R. (1996). Low-threshold Calcium currents in central nervous system neurons. *Annual Review of Physiology*, http://dx.doi.org/10.1146/annurev.physiol.58.1.329.

Izhikevich, E. M. (2003). Simple model of spiking neurons. *IEEE Transactions on Neural Networks*, *14*(6), 1569–1572. http://dx.doi.org/10.1109/TNN.2003.820440.

Johansson, R. S., & Flanagan, J. R. (2009). Coding and use of tactile signals from the fingertips in object manipulation tasks. *Nature Reviews Neuroscience*, *10*, 345–359.

Jones, L. A., & Lederman, S. J. (2007). Human hand function. *Human Hand Function*, http://dx.doi.org/10.1093/acprof:oso/9780195173154.001.0001.

Jörntell, H., Bengtsson, F., Geborek, P., Spanne, A., Terekhov, A. V., & Hayward, V. (2014). Segregation of tactile input features in neurons of the cuneate nucleus. *Neuron*, http://dx.doi.org/10.1016/j.neuron.2014.07.038.

Kasabov, N. (2010). To spike or not to spike: A probabilistic spiking neuron model. *Neural Networks*, http://dx.doi.org/10.1016/j.neunet.2009.08.010.

Kasabov, N. K. (2018). *Time-space, spiking neural networks and brain-inspired artificial intelligence (Vol. 7)*. Springer.

Kasabov, N., Scott, N. M., Tu, E., Marks, S., Sengupta, N., Capecci, E., et al. (2016). Evolving spatio-temporal data machines based on the neucube neuromorphic framework: Design methodology and selected applications. *Neural Networks*, http://dx.doi.org/10.1016/j.neunet.2015.09.011.

Lee, W. W., Kukreja, S. L., & Thakor, N. V. (2017). Discrimination of dynamic tactile contact by temporally precise event sensing in spiking neuromorphic networks. *Frontiers in Neuroscience*, *11*, 5. http://dx.doi.org/10.3389/fnins.2017.00005.

Llinás, R., & Jahnsen, H. (1982). Electrophysiology of mammalian thalamic neurones in vitro. *Nature*, http://dx.doi.org/10.1038/297406a0.

Mazzoni, A., Panzeri, S., Logothetis, N. K., & Brunel, N. (2008). Encoding of naturalistic stimuli by local field potential spectra in networks of excitatory and inhibitory neurons. *PLoS Computational Biology*, *4*(12), e1000239. http://dx.doi.org/10.1371/journal.pcbi.1000239.

Molineux, M. L., Mehaffey, W. H., Tadayonnejad, R., Anderson, D., Tennent, A. F., & Turner, R. W. (2008). Ionic factors governing rebound burst phenotype in rat deep cerebellar neurons. *Journal of Neurophysiology*, http://dx.doi.org/10.1152/jn.90427.2008.

Mountcastle, V., & Henneman, E. (2017). Pattern of tactile representation in thalamus of cat. *Journal of Neurophysiology*, http://dx.doi.org/10.1152/jn.1949.12.2.85.

Naud, R., Marcille, N., Clopath, C., & Gerstner, W. (2008). Firing patterns in the adaptive exponential integrate-and-fire model. *Biological Cybernetics*, http://dx.doi.org/10.1007/s00422-008-0264-7.

Oddo, Calogero Maria, Beccai, L., Vitiello, N., Wasling, H. B., Wessberg, J., & Carrozza, M. C. (2011). A mechatronic platform for human touch studies. *Mechatronics*, *21*(3), 604–613. http://dx.doi.org/10.1016/j.mechatronics.2011.02.012.

Oddo, Calogero M., Controzzi, M., Beccai, L., Cipriani, C., & Carrozza, M. C. (2011). Roughness encoding for discrimination of surfaces in artificial active-touch. *IEEE Transactions on Robotics*, *27*(3), 522–533. http://dx.doi.org/10.1109/TRO.2011.2116930.

Oddo, Calogero M., Mazzoni, A., Spanne, A., Enander, J. M. D., Mogensen, H., Bengtsson, F., et al. (2017). Artificial spatiotemporal touch inputs reveal complementary decoding in neocortical neurons. *Scientific Reports*, *7*, 45898.

Oddo, Calogero Maria, Raspopovic, S., Artoni, F., Mazzoni, A., Spigler, G., Petrini, F., et al. (2016). Intraneural stimulation elicits discrimination of textural features by artificial fingertip in intact and amputee humans. *ELife*, *5*, e09148. http://dx.doi.org/10.7554/eLife.09148.

Osborn, L. E., Dragomir, A., Betthauser, J. L., Hunt, C. L., Nguyen, H. H., Kaliki, R. R., et al. (2018). Prosthesis with neuromorphic multilayered e-dermis perceives touch and pain. *Science Robotics*, *3*(19), eaat3818. http://dx.doi.org/10.1126/scirobotics.aat3818.

Pruszynski, J. A., & Johansson, R. S. (2014). Edge-orientation processing in first-order tactile neurons. *Nature Neuroscience*, *17*(10), 1404–1409. http://dx.doi.org/10.1038/nn.3804.

Rongala, Udaya Bhaskar, Mazzoni, A., Chiurazzi, M., Camboni, D., Milazzo, M., Massari, L., et al. (2019). Tactile decoding of edge orientation with artificial cuneate neurons in dynamic conditions. *Frontiers in Neurorobotics*, http://dx.doi.org/10.3389/fnbot.2019.00044.

Rongala, U. B., Mazzoni, A., & Oddo, C. M. (2017). Neuromorphic artificial touch for Categorization of naturalistic textures. *IEEE Transactions on Neural Networks and Learning Systems*, *28*(4), 819–829. http://dx.doi.org/10.1109/TNNLS.2015.2472477.

Rongala, Udaya B., Spanne, A., Mazzoni, A., Bengtsson, F., Oddo, C. M., & Jörntell, H. (2018). Intracellular dynamics in cuneate nucleus neurons support self-stabilizing learning of generalizable tactile representations. *Frontiers in Cellular Neuroscience*, *12*, 210. http://dx.doi.org/10.3389/fncel.2018.00210.

Saal, H. P., Delhaye, B. P., Rayhaun, B. C., & Bensmaia, S. J. (2017). Simulating tactile signals from the whole hand with millisecond precision. *Proceedings of the National Academy of Sciences*, *114*(28), E5693–E5702. http://dx.doi.org/10.1073/pnas.1704856114.

Saarinen, A., Linne, M. L., & Yli-Harja, O. (2008). Stochastic differential equation model for cerebellar granule cell excitability. *PLoS Computational Biology*, http://dx.doi.org/10.1371/journal.pcbi.1000004.

Service, R. F. (2014). Minds of their own. *Science*, *346*(6206), http://dx.doi.org/10.1126/science.346.6206.182, 82LP–183.

Spigler, G., Oddo, C. M., & Carrozza, M. C. (2012). Soft-neuromorphic artificial touch for applications in neuro-robotics. In *Proceedings of the IEEE RAS and EMBS international conference on biomedical robotics and biomechatronics* http://dx.doi.org/10.1109/BioRob.2012.6290849.

Suresh, A. K., Winberry, J. E., Versteeg, C., Chowdhury, R., Tomlinson, T., Rosenow, J. M., et al. (2017). Methodological considerations for a chronic neural interface with the cuneate nucleus of macaques. *Journal of Neurophysiology*, http://dx.doi.org/10.1152/jn.00436.2017.

Victor, J. D., & Purpura, K. P. (1996). Nature and precision of temporal coding in visual cortex: a metric-space analysis. *Journal of Neurophysiology*, http://dx.doi.org/10.1152/jn.1996.76.2.1310.

Weber, A. I., Saal, H. P., Lieber, J. D., Cheng, J.-W., Manfredi, L. R., Dammann, J. F., et al. (2013). Spatial and temporal codes mediate the tactile perception of natural textures. *Proceedings of the National Academy of Sciences*, *110*(42), 17107–17112. http://dx.doi.org/10.1073/pnas.1305509110.

Yang, G.-Z., Bellingham, J., Choset, H., Dario, P., Fischer, P., Fukuda, T., et al. (2016). Science for robotics and robotics for science. *Science Robotics*, *1*(1), eaal2099. http://dx.doi.org/10.1126/scirobotics.aal2099.

Yi, Z., Zhang, Y., & Peters, J. (2018). Biomimetic tactile sensors and signal processing with spike trains: A review. *Sensors and Actuators, A: Physical*, http://dx.doi.org/10.1016/j.sna.2017.09.035.

Yousef, H., Boukallel, M., & Althoefer, K. (2011). Tactile sensing for dexterous in-hand manipulation in robotics - a review. *Sensors and Actuators, A: Physical*, http://dx.doi.org/10.1016/j.sna.2011.02.038.